Comparison of atmospheric tomography basis functions for point spread function reproduction

Daniel Hopkins, Richard Clare, Le Yang, Stephen Weddell
Department of Electrical and Computer Engineering
University of Canterbury

ABSTRACT

Atmospheric tomography is a process used to increase the useful sky-coverage of an adaptive optics system. The atmospheric distortion of multiple point sources are estimated using measurements from wavefront sensors. Atmospheric tomography then uses the multiple point spread functions of these guide beacons to estimate and reproduce the spatially variant point spread function for a science target that is outside the isoplanatic patch of any individual guide beacon. For imaging dynamic off-axis targets, such as satellites in low or medium Earth orbit, the increasing dimensionality of atmospheric tomography poses a problem for fast estimates of distortion in arbitrary target directions.

In this paper we simulate the performance of different basis functions in generating tomographic reproductions of point spread functions using a least-squares tomographic algorithm on standard conditions found at University of Canterbury Mount John Observatory. We measured the root mean squared error (RMSE) under identical conditions when used with Zernike polynomials, discrete cosine transforms (DCT), discrete sine transforms (DST), Haar wavelets and Daubechies-2 wavelets.

The most commonly used basis functions for tomographic reproduction are Zernike polynomials, which we found to provide high reconstruction performance, even with low numbers of modes. Our research finds that using low order DCT modes or high order Daubechies-2 wavelets have similar reconstruction results as the use of Zernike polynomials for atmospheric tomography in low noise situations, with similar RMSE values. In high noise situations, Zernike polynomials still perform the best, with the lowest RMSE up to a signal-to-noise ratio of 0.1dB. The DST showed decent noise rejection properties at higher number of modes as well.

1. INTRODUCTION

When imaging a star or other object that is effectively a point source, turbulence in the atmosphere causes aberrations in a wavefront, distorting the point spread function (PSF), and reducing the angular resolution of the imaging system [1]. The isoplanatic patch is the region around a point source where the wavefront distortion is strongly correlated to the distortion of the star's PSF. A classical adaptive optics (AO) system has poor performance when estimating the PSF for a target outside the isoplanatic patch, limiting its usefulness to within the isoplanatic patch of adequately bright stars [2].

To increase the useful sky-coverage of an adaptive optics system, atmospheric tomography can be used [3]. By measuring the atmospheric distortion of light from multiple point sources, also known as guide stars, atmospheric tomography aims to estimate the atmospheric distortion outside of the isoplanatic patches of the guide stars.

Although there are multiple different approaches of applying tomography, there is little research that has been done in how to measure distortion and correct for targets that have both temporal and spatial variance relative to the background star field, such as a satellite in low or medium Earth orbit. The Multi-Object Adaptive Optics system [4] handles off-axis targets inherently, as it corrects atmospheric distortion on multiple objects concurrently. This system has no provision for dynamic changes to the target positions, requiring on-sky calibration for generating the covariance matrices needed for reconstruction. Multi-conjugate adaptive optics also has methods that can be used for off-axis targets, but which also requires prior knowledge of target direction [5]. There has been research into using an echo state network machine learning method [2] which can correct for distortion of science targets in predetermined off-axis, anisoplanatic regions. This approach must train the echo state network for specific regions prior to correction,

so it lacks provision for dynamic changes in the target position. Single conjugated adaptive optics methods exist to improve the PSF of off-axis targets using laser guide star based adaptive optics [6], but these methods do not use atmospheric tomography to increase the effective sky coverage, nor can they be used in systems without laser guide stars.

Our proposed method for tracking a satellite involves the telescope tracking background stars at the sidereal rate, their positions remaining spatially-invariant within the image frame. As the satellite trajectory passes within an asterism of guide stars, we can use an atmospheric tomography method designed for a spatially variant target to estimate the PSF of the satellite to provide AO correction on-sky, or for later deconvolution. As the distances to satellites in Earth orbit are significantly shorter than most other astronomical science targets, satellites are often extended sources, and cannot be assumed to be a point source. By estimating the PSF using atmospheric tomography, we can estimate the distortion function for an extended target [7]. The telescope can then be moved to look in the direction of another asterism along the trajectory of the satellite, repeating the process for the duration of the pass, as shown in Fig. 1.

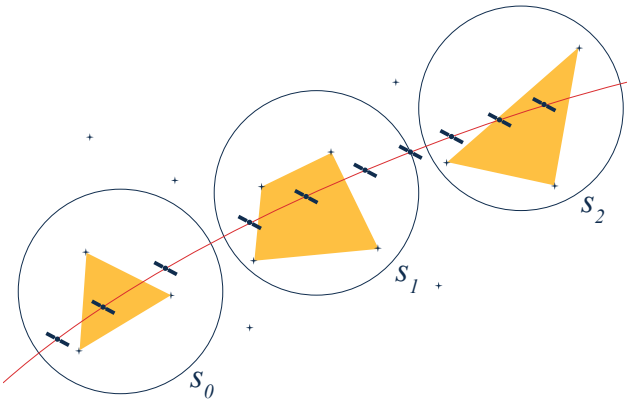

Fig. 1: Stylized view of a satellite tracking method. s_0, s_1 and s_2 are distinct viewing directions along the trajectory of the satellite. The telescope slews to one of these ahead of the satellite, initiates tomography on a constellation of stars within the view, and then waits for the satellite to pass through the viewpoint.

In this paper, we are setting out to understand the impact of basis function choice on atmospheric tomography when estimating the spatially variant PSF for off-axis science targets. Many AO systems use Zernike polynomials, as these accurately model the main optical aberrations and provide good correction even when using low numbers of optical distortion modes [8]. By understanding how different basis functions behave with different science target positions, numbers of aberration modes or measurement noise, we hope to provide a background that can be used for selecting basis functions for different atmospheric tomography use cases.

1.1 Atmospheric Tomography

Tomography is a process of imaging a higher dimensional system or object by imaging sections with the use of a penetrating wave [9]. By using the optical distortion profile of guide stars along multiple optical axes, atmospheric tomography aims to estimate the aberration for a target object along a separate optical axis, outside of the isoplanatic patch around any of the guide stars.

The tomography algorithm we have used models the atmosphere as multiple 2D layers at different altitudes perpendicular to the ground. Instead of modelling the atmosphere as a single, contiguous 3D volume, a layer-based model is sufficient to capture the effects of atmospheric turbulence on planar wavefronts, while also serving to decrease the computation required [3]. Given a constellation of natural stars being imaged from a single point on the ground, the optical pupil, or aperture, can be extended in multiple cylinders from the observation point towards each natural guide star being used, the projection of which can be seen in Fig. 2, with each cylinder of air projected onto and through a number of atmospheric layers.

Each of the projections of the telescope aperture will overlap close to the telescope, and diverge as altitude increases. This overlap between the wavefronts for each guide star can be used to estimate the distortion in the region between the isoplanatic patches of the guide stars. These measurements are used to generate a reconstruction, the tomographic

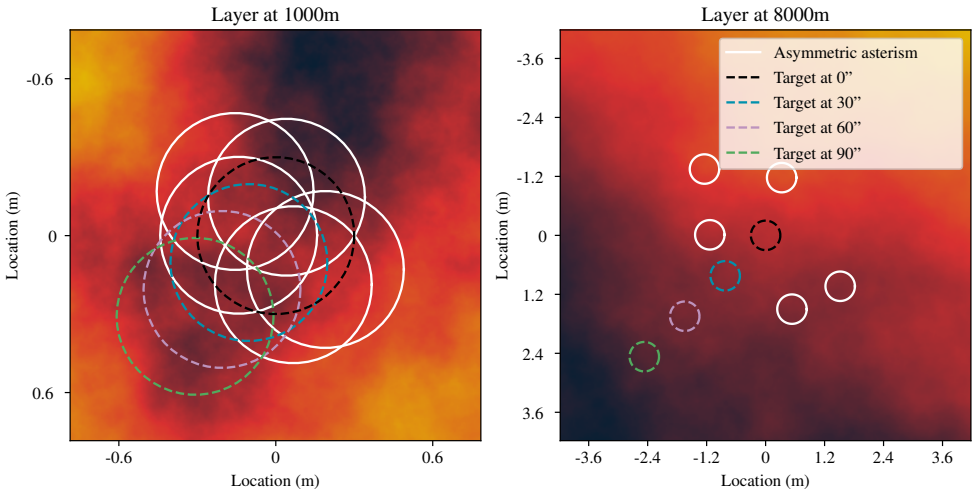

Fig. 2: Projections of telescope aperture onto atmospheric layers, for guide stars and some example targets, on layers at 1000 m (left), and at 8000 m (right).

estimate of the science target wavefront distortion.

A least-squares approximation can be used to estimate the target wavefront Zernike polynomial coefficients given the guide-star wavefronts Zernike polynomial coefficients [9]. A linear transformation of the geometry of the guide stars across multiple turbulence layers is used to map the basis function coefficients of each guide star to that of a metapupil, which fully encompasses the extent of the wavefronts for the target and all the guidestars within the field-of-view. Another linear transformation is then used to map from the wavefront of the metapupil to the target wavefront. This relationship is defined as

$$\mathbf{w_t} = \mathrm{T}\mathrm{A}^{\dagger}\mathbf{g}, \tag{1}$$

where $\mathbf{w}_t$ is a vector of N coefficients for basis function modes that define the phase screen reconstruction for the target object, and $\mathbf{g}$ is a vector of all the measured coefficients for the PSFs of the guidestars. The projection matrices, A and T, transform the basis function coefficients for any larger wavefront into a different set of basis function coefficients that model the same wavefront for a smaller circular region [10]. These matrices must be computed beforehand for any specific directions of guide stars and target object. Matrix A has size GN rows and LN columns, and T has N rows and LN columns, where G is the number of guidestars, and L is the number of atmospheric layers modelled.

1.2 Basis Functions

The atmospheric distortion of a wavefront is commonly modelled using one of several different sets of basis functions [9]. Basis functions can be used to convert a phase distortion into a set of mode coefficients. These coefficients represent the weights of a set of basis functions, and can be used to reconstruct a representation of the phase distortion using

$$\psi_r(x,y) = \sum_{n=1}^{N} a_n F_n(x,y), \tag{2}$$

where a_n is the coefficient for mode n, F_n is the basis function for mode n and N is the number of modes to be used in the reconstruction. We show some representations of an arbitrary phase screen in Fig. 3.

A phase screen representation, $\psi_r(x,y)$ from Eq. 2, is limited in how well it reproduces the ground truth phase screen, $\psi(x,y)$. As such, we have

$$r(x,y) = \psi(x,y) - \psi_r(x,y), \tag{3}$$

where $r(x,y)$ is the residual fitting error. The number of modes used in reproduction is the main limiting factor of reconstruction accuracy, as higher frequency components in the distortion require higher order modes to reproduce accurately [5].

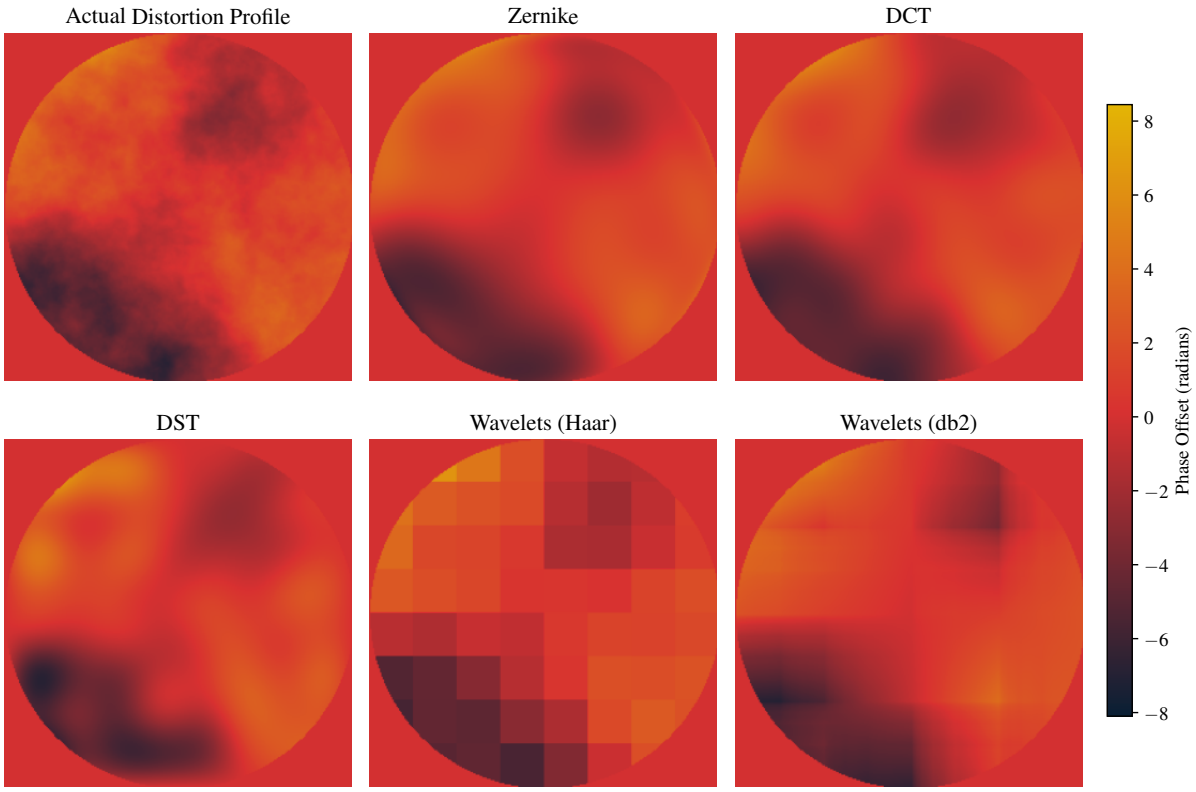

Fig. 3: Best estimate representations of a single phase screen ($D/r_0 = 6$), using different basis functions with 64 modes.

By modelling the aberration using a linear combination of functions, the dimensionality of the problem can be lowered significantly compared to dealing directly with the pixel representation of a phase screen. Even so, reducing N is important as the projection matrices A and T have $O(N^2)$ elements. The basis functions that are considered in our analysis are given in Table 1.

Table 1: The sets of basis functions analysed in these simulations.

Name	Set of basis functions
Zernike	Zernike polynomials
DCT	Cosine functions
DST	Sine functions
Wavelets (Haar)	Haar wavelets
Wavelets (db2)	Daubechies-2 wavelets

A common set of basis functions used for adaptive optics is Zernike polynomials. They are a set of orthogonal basis functions that express each of the different modes of optical aberrations [1]. With this set of functions, most of the distortion can be corrected with the lowest order Zernike modes, with residual error dropping to 10% by using up to the 5th mode Zernike polynomial [8].

The discrete cosine transform (DCT) decomposes an image into a set of cosine functions that have different frequency components in the x and y directions [11]. These can be used to reproduce the original image, and produces good results with only a small number of modes, providing effective dimensionality reduction. A similar process can be done using sine waves, using the discrete sine transform (DST). The DCT and DST are versions of the Fourier transform, that

only operate on real numbers. Some research has been done in optical tomography for biological purposes using the DCT [12], and we are adding these functions to our analysis to see if they could be used for atmospheric tomography.

Wavelets are sets of multi-scale functions that have oscillations that are finite in time, can be efficiently used to reproduce a signal with a limited range, and can provide compression and dimensionality reduction [13]. At least two wavelet families, Haar [14] and Daubechies-3 [15], have been used in atmospheric tomography research. These wavelets are discrete, allowing reconstruction from a limited number of wavelet modes. Wavelets allow the underlying matrices to have a more sparse representation [16], so higher numbers of modes may not have the same computation burden if efficient techniques for multiplying sparse matrices are used [17]. We have used Haar and Daubechies-2 wavelets as these have the filter lengths (2 and 4, respectively) that divide evenly into the pixel size of our phase screens (256) [18, 19].

1.3 Point Spread Functions

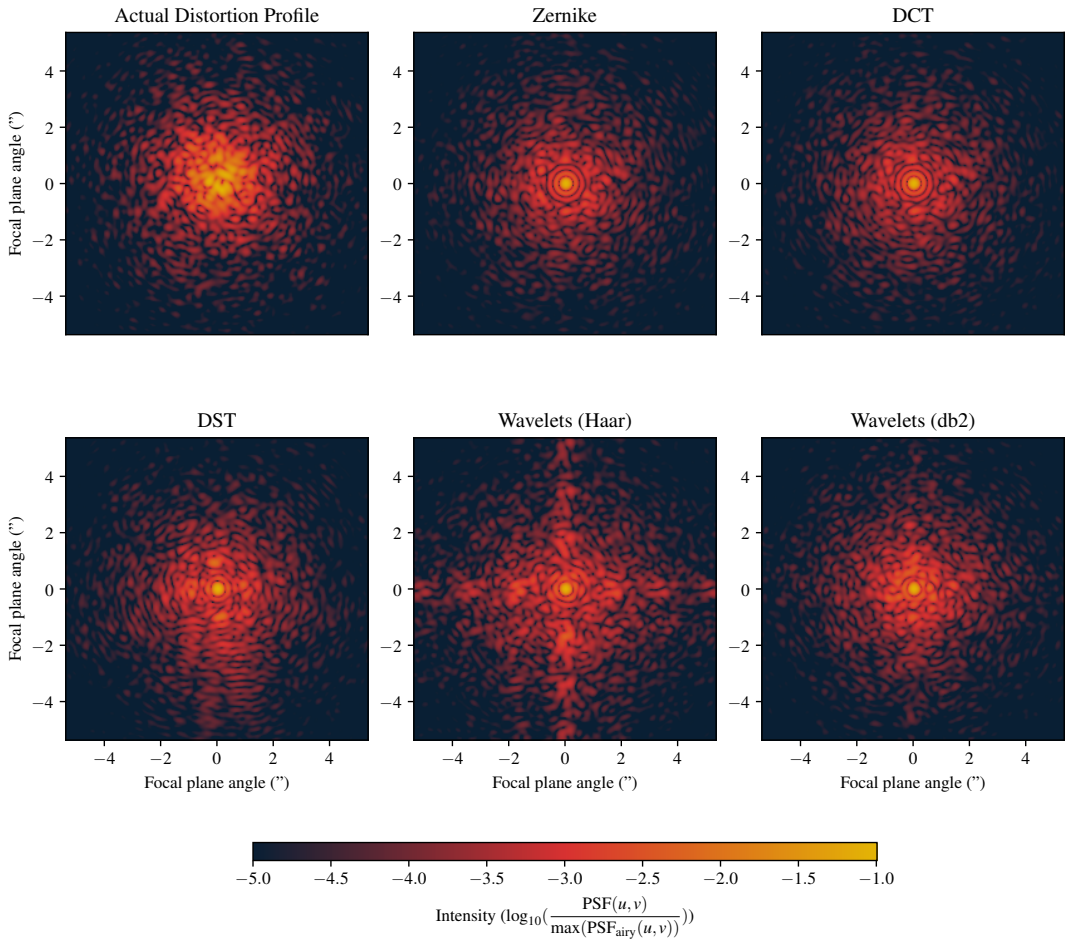

Fig. 4: Point spread functions generated from the residuals, $r(x,y)$ of different phase screen representations in Fig. 3.

A phase screen can be used to simulate atmospheric distortion, which can be used to generate the resultant PSF at the telescope focal plane by

$$\mathrm{PSF}(u,v) = \left| \mathcal{F}\left(\rho(x,y)\, e^{i\psi_r(x,y)} \right) \right|^2, \tag{4}$$

where ρ is a mask defining the telescope aperture, $\mathcal{F}$ is the 2D Fourier transform, and $\psi_r(x,y)$ is the phase screen reconstruction defined in Eq. 2. If we use the residual error, $r(x,y)$, defined in Eq. 3, instead of $\psi_r(x,y)$, we generate a PSF, such as in Fig. 4, that shows the best possible PSF we could achieve using this set of basis functions.

2. METHOD

Experiments were conducted using a simulation framework designed for comparing different tomographic algorithms in different configurations. As these experiments are intended to compare tomographic algorithms, and not other components in an adaptive optics system, we use an ideal wavefront sensor that is able to decompose a phase screen to the best possible basis function coefficients, given the basis functions satisfy the condition of orthogonality. When no noise is added the results we achieve are the best results for this atmospheric tomography algorithm using a set of basis functions, with the given number of modes. These experiments compare the tomographic output to the best estimate, which is the best possible phase screen representation of a target for a specific set of basis functions using the same number of modes. The best estimate is the equivalent of performing adaptive optics with a guide star along the same optical axis as the target.

2.1 Test Parameters

Simulations of a tomographic system were conducted using a set of environmental parameters defining the telescope and atmospheric conditions. The telescope is modelled based on the Boller and Chivens telescope at University of Canterbury Mount John Observatory (UCMJO), with an aperture diameter of 0.6m, and $f/6.5$.

The atmosphere is modelled using two layers, one at a low altitude (1000 m) and another at a higher altitude (8000 m). We used a Fried parameter, $r_0 = 10$ cm to model good seeing conditions. The wavelength of light used is 600 nm. For the atmospheric conditions at UCMJO, the isoplanatic patch is around 1 arcsecond [20].

Table 2: Constant simulation parameters, including telescope specifications and atmospheric conditions.

Parameter	Values
Telescope diameter	0.6 m
Fried parameter (r_0)	10 cm
Telescope f number	6.5
Layer altitudes	1000 m & 8000 m
Light wavelength (λ)	600 nm
Phase screen size	256 pixels

The research uses 16 and 64 modes for each basis function. These are $(2^n)^2, n \in [2,3]$, as the wavelet basis functions encode location information related to the underlying image, and require a side length of a power of 2 to have uniform performance across the entire phase screen.

Each simulation used a pair of phase screens, 50 screens in total, providing a range of different distortion profiles with an average σ of 4.36 radians. The expected value for $D/r_0 = 6$, where $\sigma^2 = 1.0299(\frac{D}{r_0})^{5/3}$ [8], is $\sigma = 4.52$ radians.

Table 3: Overview of parameters used for single simulation instances.

Test Parameter	N	Minimum	Maximum
Phase screens	50		
Basis function coefficients	2	16	64
Target angles (sets of 8)	6	5”	30”
Target angles (sets of 6)	7	40”	100”
Signal-to-noise ratio	9	20dB	0.1dB

In our results, the target position is given as a single angle measurement, the angle of the target from the major optical axis. This is the line that extends from the centre of the focal plane through the centre of the pupil plane. Testing used 8 target positions placed radially around the centre of the phase screen at each angle in steps of 5” out to 30”, then 6 positions at each angle from 40” in steps of 10” out to 100”, as shown in Fig. 5. This results in 90 different target positions.

Different guide star asterism configurations have been used in our simulations. Three symmetric asterisms use guide stars equally spaced around a specific angular radius from the major optical axis. There are two using 3 guide stars, at radii of 15” and 30”, and 6 guide stars at a 60” radius. An asymmetric asterism is also tested, which is based on

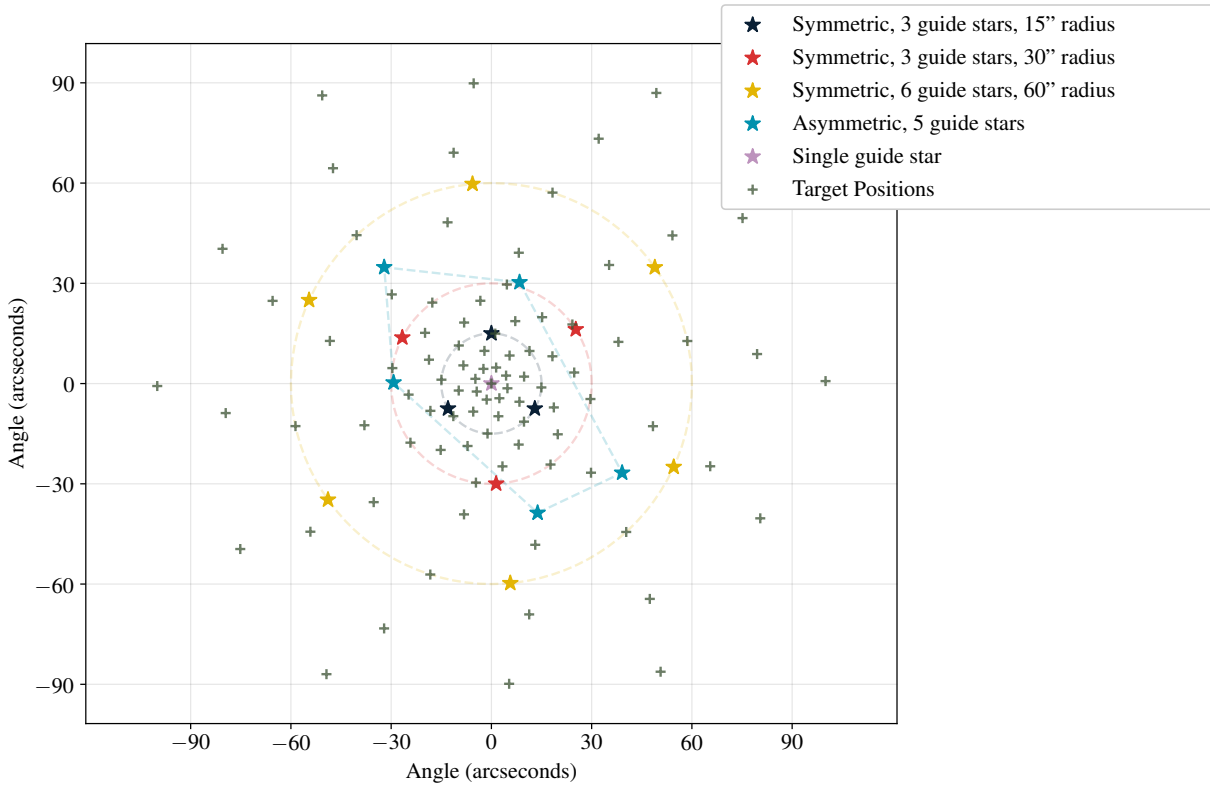

Fig. 5: Guide star asterisms and target positions used for tomography simulations.

the relative positions of 5 stars within a natural constellation. The asymmetric asterism has stars with angles of 29.3” to 47.4” from the major optical axis. We have also simulated a single guide star on the major optical axis. This is to show the difference of atmospheric tomography to the classical case of adaptive optics. The simulated asterisms are shown in Fig. 5.

Measurement noise is simulated by adding Gaussian noise to the guide star coefficients directly to the output from the wavefront sensor, that is right after basis function decomposition. By varying the value of σ for the Gaussian noise, we can measure the effect of different signal-to-noise ratios (SNRs). We simulated the target at angles of 0”, 15” and 30” for each SNR. We calculated σ for a specific set of wavefront coefficients with

$$\sigma^2 = 10^{-s/10}\left(\frac{1}{GN}\sum_{g=1}^{G}\sum_{n=1}^{N}(\mathbf{w}_{\mathbf{g}n})^2\right), \tag{5}$$

where s is the SNR in dB, and $\mathbf{w}_{\mathbf{g}_n}$ is the nth item of $\mathbf{w}_\mathbf{g}$, a vector of wavefront coefficients for guide star g of G guide stars, consisting of N mode coefficients.

2.2 Performance Metric

The performance of a tomographic algorithm is measured by calculating the root mean squared error (RMSE) between the ground truth phase screen and the tomographic reproduction. RMSE is used in simulation and bench testing, as the ground truth distortion profile is known, so the error of an adaptive optics system from the ground truth can be calculated. This metric cannot be used on sky, as there is no way of knowing the actual distortion profile of the atmosphere for comparison to the reproductions.

With the RMSE, three main error values are calculated; the tomographic reconstruction error, the best estimation error, and the error with no estimate. The tomographic reconstruction error is the error of the phase screen reproduced using the tomographic coefficients from the ground truth phase screen. The best estimate error is the error between the ground truth and the best estimated phase screen, produced using an ideal wavefront sensor with the same number of

coefficients. The no estimate error is the error if no coefficient estimation is made. This is equivalent to the error of the ground truth from a phase screen without any aberration.

RMSE gives us a metric that estimates the average error of a phase screen reconstruction from the ground truth. The RMSE is defined as

$$\varepsilon_{RMS} = \sqrt{\frac{1}{N}\sum_{n=1}^{N}(\psi_r(x,y) - \psi(x,y))^2}, \tag{6}$$

where $\psi(x,y)$ is the ground truth phase screen, and $\psi_r(x,y)$ is the reconstructed phase screen, defined in Eq. 2, and N is the number of basis function modes.

3. RESULTS

Fig. 6 shows the difference between PSFs from the best estimate phase screen representation and tomographic reconstructions. The reproductions are less well-defined compared to the ideal distortion representations, with the Zernike polynomials and DCT reconstruction PSFs lacking the distinctive central Airy disk structure that is present in the best estimate PSFs.

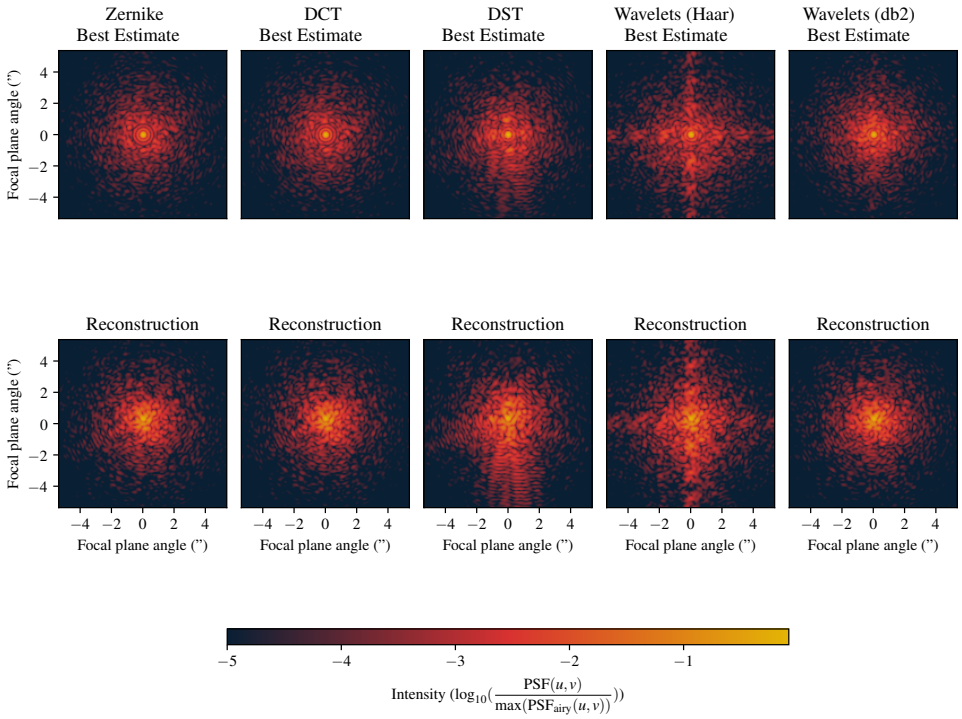

Fig. 6: Comparison of point spread functions of tomographic reconstructions to the best representation. The reconstruction is for tomography using a 3 guide star asterism at 15", a target on the major optical axis, and a phase screen with $D/r_0 = 6$.

Table 4 shows that all the basis functions can improve the RMSE of the phase screen reconstructions from that of the ground truth phase screen. For a 3 guide star, 15" radius asterism, and a target on-axis, this improvement is 47.2% in the best case, and 12.2% in the worst case. The expected best estimate for Zernike polynomials RMSE are 4.52, 0.73 and 0.40 for no estimate, 16 and 64 modes respectively [8], only slightly different to the 4.36, 0.82 and 0.48 found in our results.

It is important to note is that Zernike polynomials and the DCT both show little to no improvement when going from 16 basis function modes to 64. This is due to the lack of overlap of the telescope aperture projections on the 8000 m

Table 4: RMSE for phase screen comparisons between the different sets of basis functions given 16 or 64 modes. Shows the percentage improvement of the reconstruction over not doing any estimate. These data are for a 15”, 3 guide star asterism with the target on the main optical axis.

		RMSE (radians)		
Basis Function	Modes	Best	Reconstruction	Improvement (%)
No estimate	-	-	4.3583	-
Zernike	16	0.8169	2.3058	47.1
	64	0.4835	2.3061	47.1
DCT	16	0.8283	2.3112	47.0
	64	0.4324	2.3023	47.2
DST	16	1.8524	2.8603	34.4
	64	1.1560	2.5564	41.3
Wavelets (Haar)	16	1.5964	2.6278	39.7
	64	0.9129	2.3958	45.0
Wavelets (db2)	16	3.5764	3.8245	12.2
	64	0.8234	2.3184	46.8

layer. As this is a least squares method of tomography [9], it includes no covariance or other *a priori* modelling of atmospheric conditions. This limits the accuracy of any distortion estimates outside the projections, as higher frequency aberrations in the phase screen are not modelled. Reducing the layer angle does improve the performance when increasing the number of modes, as can be seen with the single star asterism. Performance of the 64 mode Daubechies-2 wavelets improved to a similar level as the 16 mode Zernike polynomials and DCT functions, where the RMSE improves 39.3%.

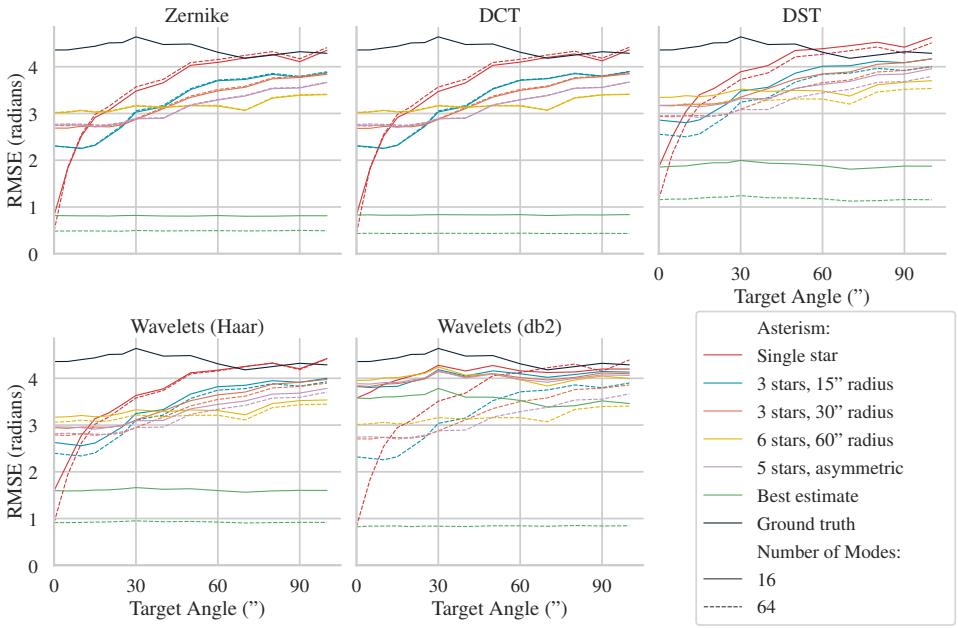

Fig. 7: RMSE values for reconstructed phase screens using different basis functions, showing the effect of target angle, asterism choice and number of modes.

In Fig. 7, it can been seen that the asterism has a strong impact on the tomography performance, with narrower asterisms showing a better minimum RMSE, and wider asterisms having a higher minimum RMSE, but remaining near to that RMSE value for a much wider angle. The RMSE stays quite constant across all target positions located within the asterism radius, before the RMSE increases towards the ground truth outside the asterism radius, which

seems to hold for all sets of basis functions tested. A single star on-axis has the best peak performance, but performs worse than any of the other asterisms beyond 20". The 5 star asymmetric asterism, with guide star angles from 29.3" to 47.4", has a similar best RMSE to the 3 star 30" radius asterism near the major optical axis, but the error increases at a slower rate beyond 30".

The choice of basis function has an effect on RMSE as well. Using Zernike polynomials and the DCT resulted in good performance at both 16 and 64 modes. There is also very little difference between these basis functions for asterism and target position performance. The two sets of wavelets, Haar and Daubechies-2, improved when going from 16 to 64 modes. The Daubechies-2 wavelets see a marked improvement in performance, showing equivalent performance to Zernike polynomials and the DCT using 16 modes. The Daubechies-2 wavelets do the worst of all basis functions at 16 modes. This is probably a limitation of these when used as basis functions, with a lack of information required to do a good reconstruction. The Haar wavelets do provide limited reproduction performance, but it isn't close to the performance given by the other sets of basis functions for the numbers of modes. The DST performs the worst overall, with performance at both 16 and 64 modes that is worse than Haar wavelets.

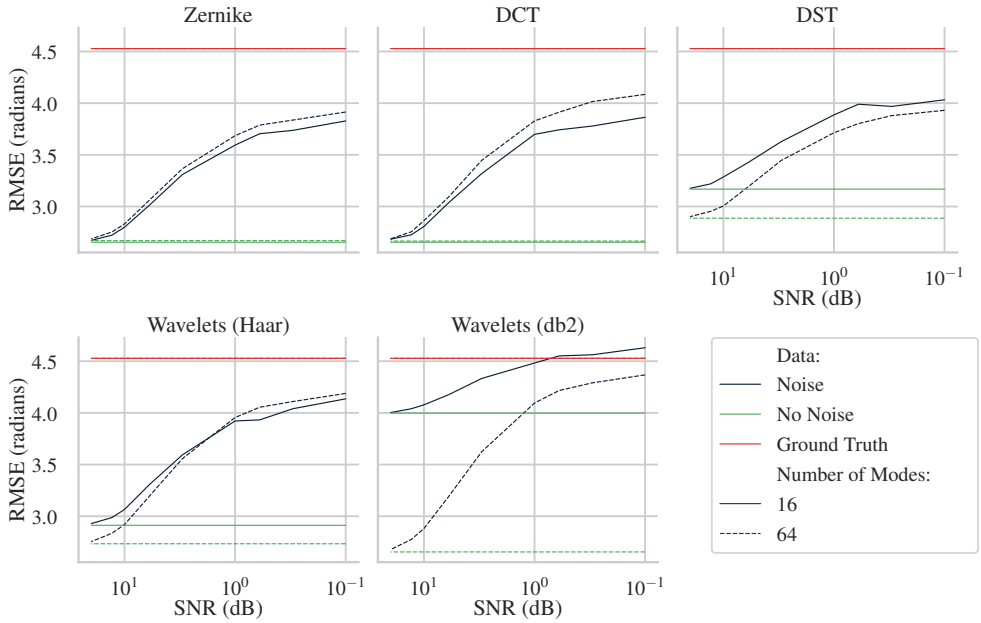

Fig. 8: RMSE for phase screen reconstructions with added noise, showing comparisons to the ground truth and the no noise cases. This plot is for a 3 guide star, 15" radius asterism. The x-axis, showing SNR (dB), is a log scale.

The effect of adding noise to the basis function mode coefficients that are used as inputs to the tomographic algorithm is shown in Fig. 8. Almost all of the sets of basis functions still show reductions in RMSE up to an SNR of 0.1dB, except 16 mode Daubechies-2. Zernike, DCT and Haar wavelets showed that 16 modes tended to have better noise rejection, and lower RMSE values.

Zernike polynomials show the lowest RMSE at every level of noise, for both numbers of modes. This is probably because the added Gaussian noise has the same sigma across all the coefficients, but Zernike polynomials are not uniform in how much they affect the wavefront correction [8]. The DCT is marginally worse, again probably due to the lower order modes having a larger correcting effect, as these are correcting low frequency components in the wavefront [12].

The DST has lower RMSE than the 64 mode DCT from an SNR of 3dB, and also to the 64 mode Haar and Daubechies-2 wavelets from around 6dB. Haar wavelets also end up with a lower RMSE than the 64 mode Daubechies-2 from 6dB. The Daubechies-2 wavelets have particularly bad noise rejection properties for this particular test. The different modes for the wavelets have a uniform effect on the resulting correction, as they also encode local spatial information [15]. Further testing to properly map measurement noise to modes with a stronger effect on reconstruction and to

simulate photon noise may show different results.

4. CONCLUSIONS

In this paper, we have set out to understand the impact of basis function choice on atmospheric tomography when estimating the spatially-variant PSF for off-axis science targets, using a least-squares estimator for tomographic reconstruction.

In low noise conditions, our results indicate that the discrete cosine transform performs similarly to Zernike polynomials, with either 16 or 64 modes, across all target angles. We suggest that DCT based methods may provide similar performance to Zernike polynomials for atmospheric tomography. The discrete sine transform (DST) performed the worst overall out of the tested basis functions in low noise conditions, and we suggest it is not a suitable choice of basis functions for tomographic applications. We found that using Daubechies-2 wavelets with higher numbers of modes begins to approach the performance of Zernike polynomials and the DCT, and with the use of proper algorithms for sparse matrices could also be a good choice for atmospheric tomography. Haar wavelets may also be useful for similar reasons, although higher order wavelets (e.g Daubechies-3 [19]) may perform better again.

In conditions with higher noise, our simulations show that lower number of modes seem to have better noise rejection. Of the sets of basis functions tested, Zernike polynomials show the best rejection of wavefront sensor measurement noise, with the lowest increase in RMSE for higher SNRs, and Daubechies-2 wavelets the worst.

Future work is to simulate and analyse the effect of photon noise, and to apply this methodology to compare different atmospheric tomography algorithms, with a focus on finding an effective method for correcting for off-axis PSFs of spatially variant target objects.

5. REFERENCES

[1] Robert K. Tyson. *Introduction to adaptive optics*, volume TT 41. SPIE Press, Bellingham, WA, 2000.

[2] Stephen J. Weddell and Russell Y. Webb. Reservoir Computing for Prediction of the Spatially-Variant Point Spread Function. *IEEE Journal of Selected Topics in Signal Processing*, 2(5):624–634, October 2008.

[3] Roberto Ragazzoni, Enrico Marchetti, and Gianpaolo Valente. Adaptive-optics corrections available for the whole sky. *Nature*, 403(6765):54–56, 2000.

[4] Fabrice Vidal, Eric Gendron, and Gérard Rousset. Tomography approach for multi-object adaptive optics. *Journal of the Optical Society of America A*, 27(11):A253, November 2010.

[5] Roland Wagner, Daniela Saxenhuber, Ronny Ramlau, and Simon Hubmer. Direction dependent Point spread function reconstruction for Multi-Conjugate Adaptive Optics on Giant Segmented Mirror Telescopes, November 2021.

[6] O Beltramo-Martin, C M Correia, E Mieda, B Neichel, T Fusco, G Witzel, and J R Lu. Off-axis point spread function characterization in laser guide star adaptive optics systems. page 15, 2018.

[7] Sierra Hickman, Vishnu Anand Muruganandan, Stephen Weddell, and Richard Clare. Image Metrics for Deconvolution of Satellites in Low Earth Orbit. In *2020 35th International Conference on Image and Vision Computing New Zealand (IVCNZ)*, pages 1–6, November 2020.

[8] Robert J. Noll. Zernike polynomials and atmospheric turbulence. *Journal of the Optical Society of America*, 66(3):207, March 1976.

[9] Roberto Ragazzoni, Enrico Marchetti, and Francois Rigaut. Modal tomography for adaptive optics. *Astronomy and Astrophysics*, 342:L53–L56, 1999.

[10] A. Tokovinin, M. Le Louarn, E. Viard, N. Hubin, and R. Conan. Optimized modal tomography in adaptive optics. *Astronomy & Astrophysics*, 378(2):710–721, November 2001.

[11] N. Ahmed, T. Natarajan, and K.R. Rao. Discrete Cosine Transform. *IEEE Transactions on Computers*, C-23(1):90–93, January 1974.

[12] Xuejun Gu, Kui Ren, James Masciotti, and Andreas H. Hielscher. Parametric image reconstruction using the discrete cosine transform for optical tomography. *Journal of Biomedical Optics*, 14(6):064003, 2009.

[13] Gregory R. Lee, Ralf Gommers, Filip Waselewski, Kai Wohlfahrt, and Aaron O'Leary. PyWavelets: A Python package for wavelet analysis. *Journal of Open Source Software*, 4(36):1237, April 2019.

[14] Peter J. Hampton, Pan Agathoklis, and Colin Bradley. A New Wave-Front Reconstruction Method for Adaptive Optics Systems Using Wavelets. *IEEE Journal of Selected Topics in Signal Processing*, 2(5):781–792, October 2008.
[15] Tapio Helin and Mykhaylo Yudytskiy. Wavelet methods in multi-conjugate adaptive optics. *Inverse Problems*, 29(8):085003, August 2013.
[16] Ronny Ramlau and Bernadett Stadler. An augmented wavelet reconstructor for atmospheric tomography, November 2020.
[17] Di Yan, Tao Wu, Ying Liu, and Yang Gao. An efficient sparse-dense matrix multiplication on a multicore system. In *2017 IEEE 17th International Conference on Communication Technology (ICCT)*, pages 1880–1883, October 2017.
[18] Ingrid Daubechies. *Ten lectures on wavelets /*. CBMS-NSF regional conference series in applied mathematics. Society for Industrial and Applied Mathematics,, 1992.
[19] Mykhaylo Yudytskiy, Tapio Helin, and Ronny Ramlau. Finite element-wavelet hybrid algorithm for atmospheric tomography. *Journal of the Optical Society of America A*, 31(3):550, March 2014.
[20] Judy Lynette Mohr. Atmospheric Turbulence Characterisation Using Scintillation Detection and Ranging. 2009.